

# Electroless Nanoplatinating of Iridium: Template-Assisted Nanotube Deposition for the Continuous Flow Reduction of 4-Nitrophenol

Martin Christoph Scheuerlein,<sup>\*,[a]</sup> Falk Muench,<sup>[a]</sup> Ulrike Kunz,<sup>[a]</sup> Tim Hellmann,<sup>[b]</sup> Jan P. Hofmann,<sup>[b]</sup> and Wolfgang Ensinger<sup>[a]</sup>

Electroless plating is a powerful tool in nanofabrication and is available for many of the noble transition metals. There is, however, a striking lack of electroless plating procedures for the rarer platinum-group metals. In this work, two plating baths for nanoscale iridium coatings are developed and their conformality and nanofabrication potential are showcased by coating ion-track-etched polycarbonate membranes, creating Ir nanotubes in the process. Both plating solutions yield morphologically different deposits, indicating that the microstructure of the film can be tuned by adjusting the composition of the plating bath. The catalytic performance of the deposited materials is

investigated by using membrane-embedded nanotubes as catalysts for the reduction of 4-nitrophenol and methyl orange by borohydride, showing remarkable activity and stability. Operation in flow-through configuration, in which the metalized membrane is implemented as a microreactor greatly enhances the interaction with the catalyst surface, considerably increasing product yield. The results highlight the potential of Ir nanoplatinating for realizing sophisticated nanostructures and heterogeneous catalysts, but also illustrate the intricacies related to the complex chemistry of electroless Ir plating baths.

## 1. Introduction

Iridium as a platinum-group transition metal is of great interest for a variety of key applications, mainly due to its high thermal and remarkable chemical stability, electric conductivity, pronounced Spin-Hall effect and catalytic activity.<sup>[1,2]</sup> Potential and established uses range from protective coatings<sup>[3]</sup> and spintronic devices<sup>[2]</sup> to catalyst and electrode materials for a wide variety of reactions including methanol oxidation,<sup>[4]</sup> water splitting<sup>[5–10]</sup> and hydrazine decomposition, e.g. in monopropellant rocket engines.<sup>[11,12]</sup> Ir nanoparticles (NPs) and thin-films are of particular interest for these catalytic applications since their increased surface-to-volume ratio allows for a more efficient noble metal utilization.<sup>[7]</sup> While dispersed Ir NPs are often prepared by wet-chemical methods,<sup>[13–16]</sup> Ir thin films can be deposited by various techniques including electroplating,<sup>[9,17–19]</sup> pulsed laser deposition,<sup>[20,21]</sup> chemical vapor deposition<sup>[22]</sup> and atomic layer deposition (ALD).<sup>[5,23,24]</sup> Other synthesis routes rely


on drying Ir NP dispersions on solid substrates<sup>[10,14]</sup> or the utilization of reductive substrates such as porous carbon.<sup>[25]</sup>


In general, for catalytic applications it is often beneficial to attach NPs to high surface area support structures, e.g. fiber networks<sup>[26]</sup> or porous membranes such as anodic aluminum oxide (AAO)<sup>[5,27]</sup> and ion-track etched polymers.<sup>[28]</sup> The latter have gained increasing research interest due to their versatility regarding pore shape, dimensions and areal density.<sup>[29]</sup> Coated membranes can be used as static catalysts,<sup>[30,31]</sup> implemented as flow-reactors<sup>[28,32]</sup> or as templates to fabricate stand-alone 1D nano-objects such as nanotubes or -wires,<sup>[33–35]</sup> as well as arrays<sup>[36]</sup> or free-standing networks thereof.<sup>[37–39]</sup> Unfortunately, applying uniform coatings to these complex substrates is challenging for many thin film deposition techniques. Recent advances in Ir-ALD have enabled the uniform and smooth coating of AAO-membranes.<sup>[5]</sup> These processes, however, are limited to substrates that can endure the high temperatures and oxidizing chemical environment present in most ALD reactions.<sup>[23,24]</sup> Furthermore, it requires complicated and expensive vacuum equipment as well as the handling of H<sub>2</sub>, O<sub>2</sub> and/or O<sub>3</sub> gas.

Wet-chemical methods like electroplating and electroless plating can often be performed under ambient conditions, are generally cheaper to set up and can be scaled up more easily. While electroplating is limited to conductive substrates, electroless plating has proven to be particularly suitable for the conformal metal coating of various materials (including insulators) and complex substrates.<sup>[40–42]</sup> In electroless plating, metal ions are reduced by a reducing agent in an autocatalytic reaction without an external supply of electrons.<sup>[43]</sup> While most industrial electroless plating procedures focus on Ni deposits and are usually optimized for the fast coating of macroscale

[a] M. C. Scheuerlein, Dr. F. Muench, U. Kunz, Prof. Dr. W. Ensinger  
Technical University of Darmstadt, Department of Materials and Earth  
Sciences, Alarich-Weiss-Strasse 2, 64287 Darmstadt, Germany  
E-mail: scheuerlein@ma.tu-darmstadt.de

[b] T. Hellmann, Prof. Dr. J. P. Hofmann  
Technical University of Darmstadt, Surface Science Laboratory, Department  
of Materials and Earth Sciences, Otto-Berndt-Strasse 3, 64287 Darmstadt,  
Germany

 Supporting information for this article is available on the WWW under  
<https://doi.org/10.1002/celec.202000811>

 © 2020 The Authors. Published by Wiley-VCH GmbH. This is an open access  
article under the terms of the Creative Commons Attribution Non-  
Commercial NoDerivs License, which permits use and distribution in any  
medium, provided the original work is properly cited, the use is non-  
commercial and no modifications or adaptations are made.

workpieces,<sup>[44,45]</sup> plating reactions suitable for nanomaterial production have been published for a variety of metals including Cu,<sup>[35]</sup> Ag,<sup>[32,38,46–48]</sup> Au,<sup>[49,50]</sup> Pd,<sup>[51–54]</sup> and Pt.<sup>[35,53,55]</sup> Aside from producing nanoscale films, electroless deposition is also a promising approach for depositing NPs onto various substrates.<sup>[56]</sup>

However, reports on wet-chemical, let alone electroless plating of Ir films are very rare.<sup>[43]</sup> A 1997 US patent application proposes a reaction system based on hydrazinium complexes of Ir.<sup>[57]</sup> Another report studies the growth of Ir NPs on ITO wafers by submerging the substrate in a solution containing Ir(III) and NaBH<sub>4</sub>.<sup>[14]</sup> However, in this case, the desired plating reaction is accompanied by considerable homogeneous nucleation of Ir NPs in the bulk solution, and the obtained deposits mostly consist of isolated particles, i.e. no cohesive NP film is formed.<sup>[14]</sup>

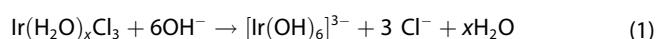
For the plating solution to be more surface-selective, certain requirements have to be met: (i) Ir-ions that are not in contact with the substrate or already grown NP film have to be stable in solution for the duration of the plating reaction, despite the presence of large amounts of reducing agent. (ii) Since most reducing agents employed in electroless plating benefit from or even require alkaline conditions,<sup>[58]</sup> hydrolysis of the Ir species and resulting formation of insoluble IrO<sub>2</sub> precipitates has to be sufficiently suppressed.<sup>[13]</sup> (iii) The energy barrier for self-nucleation of Ir-particles has to be higher than for growth on existing Ir surfaces. It has been suggested that this is not the case in certain systems.<sup>[59]</sup>

Based on these requirements, we outline the development of two electroless Ir plating baths suitable for the deposition of Ir NP films. We demonstrate the conformality of our reaction by coating ion-track etched polycarbonate membranes as a challenging 3D-substrate characterized by a high surface area and recessed pores of high aspect-ratio, creating Ir nanotubes in the process. To our best knowledge, this is the first report on electrolessly plated Ir nanotubes. Using the reduction of 4-nitrophenol and methyl orange (MO) as model reactions,<sup>[60,61]</sup> we investigate the stability and activity of our nanotube arrays as heterogeneous catalysts.

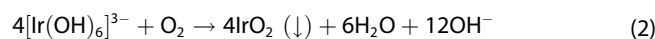
## 2. Results and Discussion

### 2.1. Development of Ir Nanoplatin Solutions

Ir(III) chloride hydrate (Ir(H<sub>2</sub>O)<sub>x</sub>Cl<sub>3</sub>) is chosen as the starting compound because of its good availability and solubility in water.<sup>[1]</sup> As a popular precursor for many Ir complexes its behavior in aqueous solutions has been studied in detail in the literature.<sup>[62–64]</sup> Briefly, after being dissolved in water, the mixed aqua-chloro-complex undergoes hydrolysis (**Equation (1)**), the speed of which depends largely on temperature and the pH of the solution.<sup>[62]</sup>



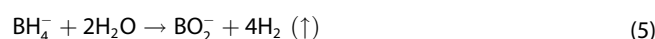
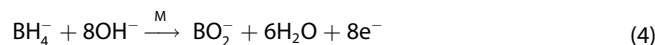
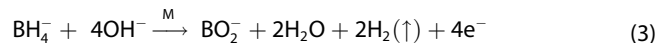
It has been shown that in the presence of dissolved oxygen the hydrolysis and oxidation of Ir(III) results in the formation of insoluble IrO<sub>2</sub> precipitates with a characteristic blue-black color (**Equation (2)**).<sup>[64,65]</sup>



Since this process can be accelerated by UV-irradiation, Ir (III)-containing solutions should be protected from direct sunlight during handling and storage.<sup>[64]</sup>

Due to their comparatively high reduction potential (Ir<sup>3+</sup> + 3e<sup>-</sup> → Ir<sup>0</sup>; 1.156 V vs. SHE<sup>[1]</sup>), reducing Ir ions to metallic form should be clearly feasible with most common reducing agents employed in electroless plating.<sup>[66]</sup> However, it was found that due to the kinetic inertness of most Ir complexes, only strong reductants like borohydrides, often applied in large excess, can reduce Ir ions in ambient conditions.<sup>[13]</sup> A similar unusual stability against reduction has been observed in Ru(III) complexes<sup>[67]</sup> and might be the underlying reason for the lack of electroless plating procedures for the more exotic noble metals Ru, Rh, Os and Ir. Likewise, Ir electrodeposition was found to suffer from extremely low Faradaic efficiency and excess H<sub>2</sub> formation.<sup>[19]</sup>

Due to the limited choice of suitable reducers, NaBH<sub>4</sub> has become popular in the synthesis of Ir NP dispersions and agglomerates (sponges).<sup>[13–16,68]</sup> A possible mechanism for the anodic oxidation of NaBH<sub>4</sub> in the presence of a metal catalyst is given by *van den Meerakker*.<sup>[58]</sup> Briefly, at the metal surface, the hydride ligands of the borohydride anions are successively oxidized and replaced by OH<sup>-</sup>. This results in products of the type BH<sub>3-x</sub>(OH)<sub>x</sub><sup>-</sup>, ending with metaborate (BO<sub>2</sub><sup>-</sup>). In summary, two overall reactions can be formulated, the dominant one is determined by the solution pH (**Equation (3)**, **(4)**).<sup>[58]</sup> A third competing reaction is the dehydrogenation of NaBH<sub>4</sub> due to hydrolysis (**Equation (5)**).<sup>[69,70]</sup> Its reaction rate is influenced by pH and generally lower in alkaline environments.<sup>[70]</sup> Still, a significant amount of borohydride is converted via this reaction path, making it necessary to regularly add NaBH<sub>4</sub> during the plating reaction.



In electroless plating, complexing agents are usually added to stabilize the precursor ions, preventing homogeneous NP nucleation.<sup>[43]</sup> Together with the reducing agent the obtained complexes form a metastable redox pair which reacts only at catalytically active surfaces and then proceeds autocatalytically on the deposited NP film. In this study, trisodium citrate (Na<sub>3</sub>Citr) and ethylenediamine (EDA) are investigated as possible stabilizers to achieve this state of metastability as long as possible over the course of the Ir-plating reaction.

## 2.1.1. Citrate-Stabilized Plating Solution

Citrates are a popular choice for the stabilization of metal plating baths due to their low cost and low toxicity. They are often used in the plating of iron group metals, especially Ni.<sup>[34,44]</sup> Depending on the central ion and external factors like solution pH, citrate anions usually form mono- or dinuclear chelate-type complexes that are often mixed with other ligands.<sup>[71,72]</sup> In the present case, citrate is added in large excess and the solution is aged at elevated temperature in order to minimize the presence of mixed complexes and maximize the stability of the solution. These precautions are necessary due to the aforementioned unusual inertness of many Ir(III) complexes which suffer from slow ligand exchange under ambient conditions.<sup>[73]</sup> Additionally, lowering the pH by adding HCl presumably slows down hydrolysis and resulting unwanted side reactions like IrO<sub>2</sub> formation during the heat-treatment. It has been reported that adding small amounts of HCl does not lead to an additional

chlorination of Ir(III) aqua-chloro-complexes,<sup>[74]</sup> suggesting its function in our case is purely pH related. This is further corroborated by our own reference measurement of IrCl<sub>3</sub> dissolved and heated in 10 M HCl, showing a vastly different absorbance spectrum than the plating solutions which utilize a much lower HCl concentration (see supporting information, Figure S1).

Figure 1a shows UV-Vis spectra of Ir(H<sub>2</sub>O)<sub>x</sub>Cl<sub>3</sub> solutions with and without citrate. Due to the strong absorbance in the UV-region, solutions were diluted in a 1:100 ratio with respect to the concentrations given in Table 1. In accordance to an earlier report, without additional heat input no changes in absorbance above 250 nm are observed when citrate is added.<sup>[14]</sup> This indicates that little to no ligand exchange or further hydrolysis occurs in ambient conditions. The increase in absorbance below 250 nm can be attributed mainly to dissolved trisodium citrate, as indicated by a reference measurement. During heat treatment, the broad shoulder peak between 250–350 nm, which is

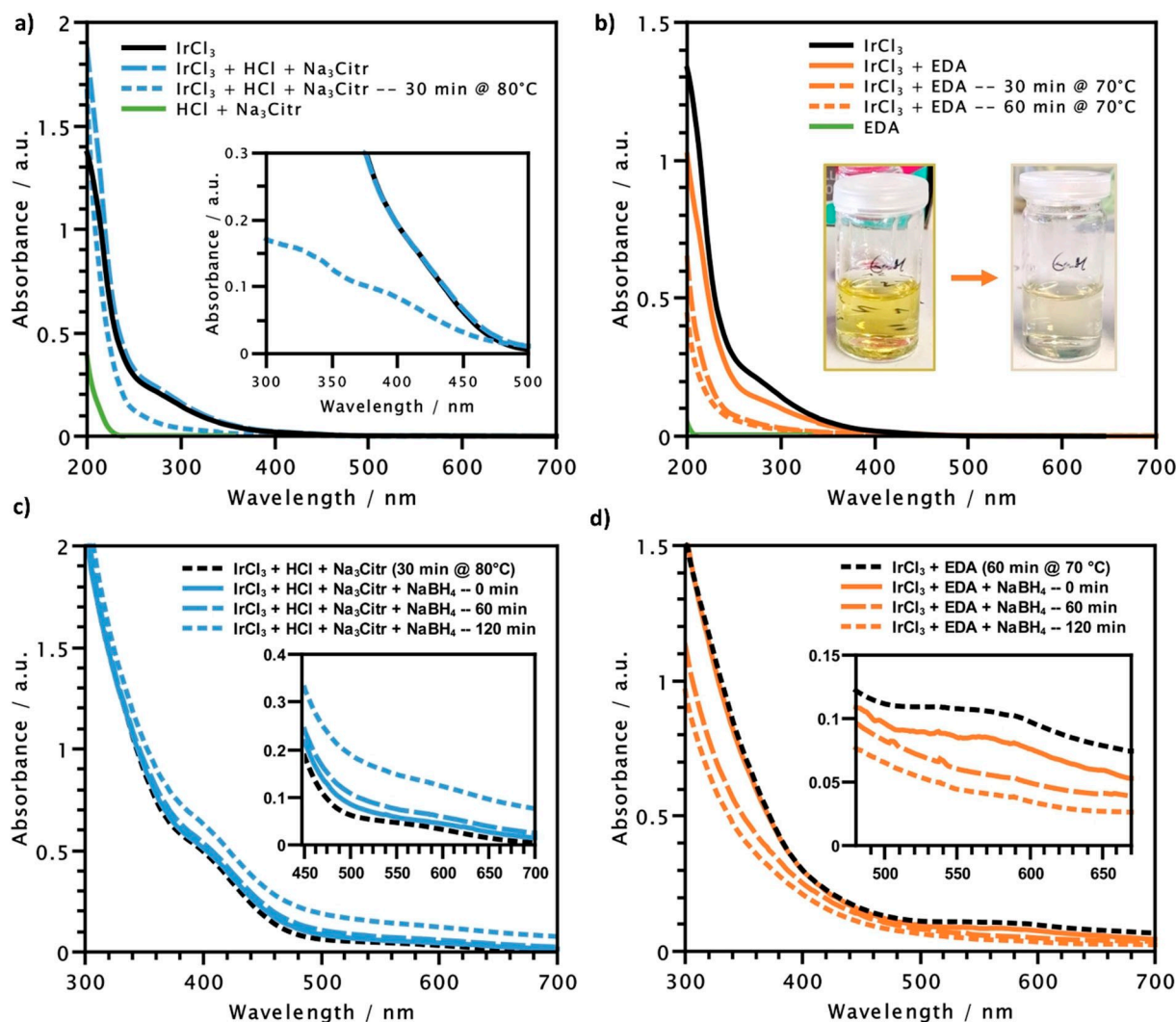


**Figure 1.** UV-Vis spectra of IrCl<sub>3</sub>-solutions before and after addition of a) trisodium citrate (Na<sub>3</sub>Citr) and b) EDA, diluted 1:100 and 1:50, respectively. This is necessary due to the strong absorbance in the UV-range. The inset in (a) shows a magnification of the visible range before and after citrate addition and heat treatment. The images in (b) show the color change of the EDA-containing solution caused by ligand exchange. Subfigures (c, d) show UV-Vis spectra of the (undiluted) citrate- and EDA-stabilized plating baths before and after the addition of NaBH<sub>4</sub>.

frequently observed in  $\text{Ir}(\text{H}_2\text{O})_x\text{Cl}_{3-x}$ -solutions and attributed to spin-allowed  $\pi \rightarrow \pi^*$  transitions from water ligands disappears,<sup>[75]</sup> indicating a replacement of  $\text{H}_2\text{O}$  by other ligands. The as-prepared solution also shows a faint shoulder peak around 400 nm (see inset Figure 1a) which is difficult to trace back to a single origin due to its width. According to previous reports, absorbances in that range can be attributed to metal-to-ligand ( $\text{Ir}(\text{III}) \rightarrow \text{Cl}^-$ ) charge transfer bands in mixed aqua-chloro- and hydroxo-chloro-complexes of  $\text{Ir}(\text{III})$ , where longer wavelengths indicate the presence of more chlorinated compounds.<sup>[15,74]</sup> After annealing, the absorbance in this range decreases significantly, suggesting that most of the  $\text{Cl}^-$  is replaced by  $\text{OH}^-$  and/or citrate. Two faintly remaining peaks around 330 nm and 390 nm indicate that small amounts of both hydrolyzed and chlorinated  $\text{Ir}(\text{III})$  compounds are still present in the solution after heat treatment.<sup>[74]</sup>

Figure 1c shows UV-Vis spectra of the undiluted solution before and after the addition of  $\text{NaBH}_4$ , which corresponds to the assembly of the final electroless plating bath. In case of the citrate stabilized solution, adding the reducing agent does not cause much change to the spectrum, suggesting that the coordination environment of the Ir ions remains unchanged during the plating reaction. A broad and very faint shoulder peak can be observed, centered around 560 nm. It was previously observed in aqueous  $\text{Ir}(\text{III})$  and  $\text{Ir}(\text{IV})$  solutions, with and without the addition of citrate.<sup>[16,74]</sup> Reference measurements of a freshly prepared aqueous  $\text{IrCl}_3$  solution, as well as an  $\text{IrCl}_3$  solution with tremendous HCl excess – which should strongly favor chlorination and impede oxide formation – also show similar absorbance behavior in this range (see supporting information, Figure S11). Considering the contribution of possible  $\text{IrO}_2$  precipitates, considerable differences are apparent in peak shape and position compared to both our own measurements and previous reports on  $\text{IrO}_2$  particle dispersions.<sup>[13,64,65]</sup> This strongly suggests that, in the present case, the absorbance is not caused by precipitating  $\text{IrO}_2$ . As time progresses, there is a slight increase in absorbance over the whole spectrum. Apart from  $\text{H}_2$  bubble formation caused by decomposing  $\text{NaBH}_4$ , this might be attributed to the onset of homogeneous Ir NP nucleation.

### 2.1.2. EDA-Stabilized Plating Solution

EDA (en, when referred to as a ligand) is a usually bidentate chelating ligand that has been successfully employed as a complexing agent in the electroless deposition of other noble metals including Ag,<sup>[32]</sup> Pd<sup>[76]</sup> and Pt.<sup>[37,54]</sup> Similar to Pt(IV) it is expected that  $\text{Ir}(\text{III})$ -ions form en-complexes of the type  $[\text{Ir}(\text{en})_x\text{L}_{(6-2x)}]^{(2x-3)}$  with  $x=0-3$ .<sup>[54,77-80]</sup> Here, 'L' denotes other ligands, which in the present system are likely  $\text{OH}^-$  and/or  $\text{Cl}^-$ . The degree of complexation can be tuned by adjusting the molar ratio between EDA and  $\text{Ir}(\text{III})$ .<sup>[77]</sup> In order to thermally activate the process and promote maximum en-complexation, the mixture is heated to 70 °C for 60 min while EDA is provided in 2-fold excess (molar ratio 6:1, EDA:Ir). During heat-treatment, the solution becomes more and more colorless (see images in

**Table 1.** Composition of the Ir NP film plating baths discussed in this study. The hydrated  $\text{Ir}(\text{III})$  chloride is treated as monohydrate for concentration calculations.

	Solution 1 (citrate stabilized)	Solution 2 (EDA stabilized)
$\text{IrCl}_3 \cdot x\text{H}_2\text{O}$	5 mM	3 mM
EDA	–	18 mM
$\text{Na}_3\text{C}_6\text{H}_5\text{O}_7 \cdot 2\text{H}_2\text{O}$	20 mM	–
HCl	15 mM	–
$\text{NaBH}_4$	50 mM (added hourly)	60 mM (added hourly)

Figure 1b), which can also be observed during the complexation of  $\text{Ir}(\text{III})$  with  $\text{NH}_3$ , a similar amine-based ligand.<sup>[81]</sup> UV-Vis spectra of the solutions before and after EDA addition are shown in Figure 1b. Measurements were performed on solutions diluted in a 1:50 ratio compared to the concentrations given in Table 1. In contrast to the citrate-containing solutions discussed before, a change in UV-Vis absorbance can be detected without additional heat input (Figure 1b). This is likely due to the significant increase in pH ( $\sim \text{pH } 4 \rightarrow \sim \text{pH } 9$ ) caused by the addition of EDA and resulting hydrolysis of  $\text{Ir}(\text{III})$ . During heat treatment, the absorbance in the visible and near-UV range decreases, indicating the ongoing replacement of existing ligands by en.<sup>[78]</sup> A similar observation is made during the en-complexation of  $[\text{PtCl}_6]^{2-}$ .<sup>[54]</sup>

Figure 1d shows UV-Vis spectra of the undiluted EDA-stabilized solution before and after the addition of  $\text{NaBH}_4$ . Similar to the citrate-containing plating bath, initially a very faint shoulder peak around 560 nm can be observed, in accordance to our own measurements and previous reports on aqueous  $\text{IrCl}_3$  solutions.<sup>[16,74]</sup> Just adding  $\text{NaBH}_4$  does not cause significant changes to the UV-Vis spectrum. However, over time the absorbance in the 300–400 nm range decreases, which may be an indication that the complexation reaction between Ir and EDA is still in progress, despite the previous heat treatment. Interestingly, the faint shoulder peak around 560 nm also weakens with time. This indicates, that during the deposition no  $\text{IrO}_2$  NPs are formed and further consolidates the assumption that the initial absorbance in this range is not caused by precipitated  $\text{IrO}_2$ , but rather by remaining chlorinated  $\text{Ir}(\text{III})$ - and  $\text{Ir}(\text{IV})$ -species that experience a change in their coordination environment or are reduced during the plating reaction. Additionally, a previous report suggests that  $[\text{Ir}(\text{OH})_6]^{3-}$  intermediates, which show characteristic absorbance around 320 nm, are a prerequisite for the formation of  $\text{IrO}_2$  in aqueous solutions.<sup>[64]</sup> In our case, during both the heat treatment and plating reaction no specific increase in absorbance can be observed in that range. Furthermore, in contrast to the citrate-stabilized bath, no overall rise in absorbance can be observed over the course of 120 min, indicating a higher stability of the EDA-stabilized plating solution in regard to homogeneous Ir NP formation.



## 2.2. Electroless Deposition of Ir NP Films

Ir NP films are deposited in ion-track etched polymer membranes using the previously discussed plating solutions. Figure 2a shows a schematic representation of the steps leading to the formation of an Ir NP film. In order to initiate the autocatalytic plating reaction, a layer of Pd seeds is deposited on the polymer surface by a two-step sensitization and activation procedure, which has been described elsewhere.<sup>[34]</sup> In short, during sensitization Sn(II) ions electrostatically attach to polar functional groups on the polycarbonate surface (Figure 2a, step 1). The membranes are then transferred to a Pd(II) solution where the adsorbed Sn(II) reduces Pd(II) to form Pd NPs (Figure 2a, step 2). Pd is chosen as a seed material because of its high catalytic activity towards the oxidation of NaBH<sub>4</sub><sup>[66]</sup> and its previous successful use as a substrate for Ir layers.<sup>[59]</sup> After seeding, the membranes are submerged in the plating solution (Figure 2a, step 3). From the beginning, both plating reactions are accompanied by strong gas evolution, indicating that in both cases a significant amount of borohydride is converted in reactions involving the formation of H<sub>2</sub> (Equation (4) and (6)). As both the Pd and Ir NPs as well as metal-ions in solution can catalyze the hydrolysis of borohydride (Equation (6)),<sup>[70]</sup> it is to assume that a considerable amount of NaBH<sub>4</sub> is “lost” without participating in the Ir reduction reaction.

Homogeneous nucleation starts becoming noticeable after roughly 3–4 h in the citrate stabilized solution as indicated by the dark grey color of dispersed Ir NPs. This is an increase in bath stability by a factor of 1.5–2 compared to preliminary experiments using the same Ir(III)-concentration without adding citrate. In order to avoid Ir-particles blocking the pores of the membrane, the plating bath is exchanged every 3 h. The EDA stabilized solution does not show obvious signs of homoge-

neous Ir particle formation even after 6 h of plating. However, the solution is replaced after that duration to avoid depletion of Ir. As shown in Figure 2b, during plating the membranes become increasingly darker and the initial brown color caused by the Pd seeds turns black. This indicates the deposition of a thin Ir NP layer on top of the Pd seeds. The absence of a metallic sheen suggests that the deposited film is very thin, as thicker layers tend to adopt the shiny appearance of the respective bulk metal.

The obtained deposits are analyzed in scanning electron microscopy (SEM) before and after removal of the PC membrane (Figure 3). Both plating reactions leave the substrate evenly coated with a thin layer of NPs (Figure 3a, b). The citrate-deposit appears rough and foam-like, while the EDA-deposition leads to the formation of a smooth and dense particle film. After dissolving the PC membrane in dichloromethane (DCM), tube fragments with lengths of several μm remain (Figure 3c–f). This confirms that the deposited NPs are interconnected and form a cohesive layer. However, the obtained tubes are not entirely self-supporting and require the polymer matrix to fully maintain their delicate structure. The template-facing surface of the tubes is remarkably smooth and thus shows a particularly good reproduction of the complex template geometry. Measuring the film thickness at the tube openings yields 20 ± 5 nm and 45 ± 17 nm for the EDA and citrate deposits, respectively. This suggests that the deposition rate from the citrate bath is significantly higher than from the EDA-stabilized solution, in agreement with the higher reactivity observed in terms of bath stability and lifetime. EDS spectra recorded alongside SEM (Figure 3g, h) confirm the presence of Ir in both deposits. Sn and Pd peaks result from the sensitization and activation procedure prior to Ir deposition. The presence of oxygen can be attributed to the formation of SnO<sub>x</sub> during activation, residues of the PC membrane and/or a superficial oxidation of Pd and/or Ir. The large Si peak is caused by the sample holder.

Cross-sections of the deposited tubes prepared parallel (Figure 4a, b) and perpendicular (Figure 4c–f) to the membrane surface are analyzed in transmission electron microscopy (TEM). Both films consist of roughly spherical NPs with diameters below 10 nm (Figure 4e, f). The citrate deposit shows a comparatively narrow particle size distribution around an average value of 3.9 ± 1.1 nm (Figure 4g). Similar particle sizes have been reported for colloidal Ir NPs that were formed by homogeneous nucleation in the presence of citrate.<sup>[16]</sup> It might be possible that in this case citrate takes on a dual-role of both stabilizing Ir(III)-ions in solution while simultaneously acting as a growth limiting capping agent during NP formation. However, the borohydride-driven formation of sponge-like assemblies of similarly sized NPs has been observed for Ir and several other noble metals without the use of any additives.<sup>[13,68]</sup> This suggests that the lower stability of the solution generally favors the formation of new Ir NPs over the growth of existing ones, leading to the formation of structures that more closely resemble those obtained by homogeneous nucleation.

Deposits from the EDA-stabilized solution exhibit a wider particle size distribution and a larger mean diameter of 6.8 ± 2.0 nm (Figure 4h). The larger average particle size and the

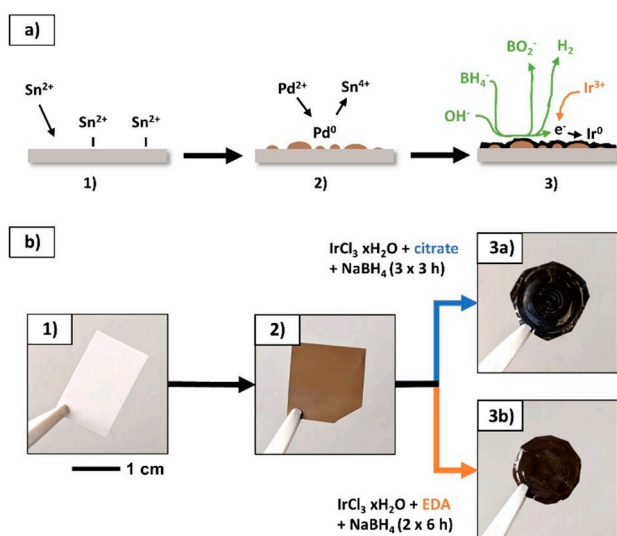


**Figure 2.** a) Schematic representation of electroless Ir-deposition. 1) Adsorption of Sn(II) on the polymer surface; 2) reduction of Pd(II) by Sn(II), formation of Pd NPs; 3) reduction of Ir(III) on the surface by oxidation of borohydride. b) Photographs of the PC membrane: 1) pristine, 2) after Pd-seeding, 3a, 3b) after Ir deposition from citrate- and EDA-stabilized baths, respectively.

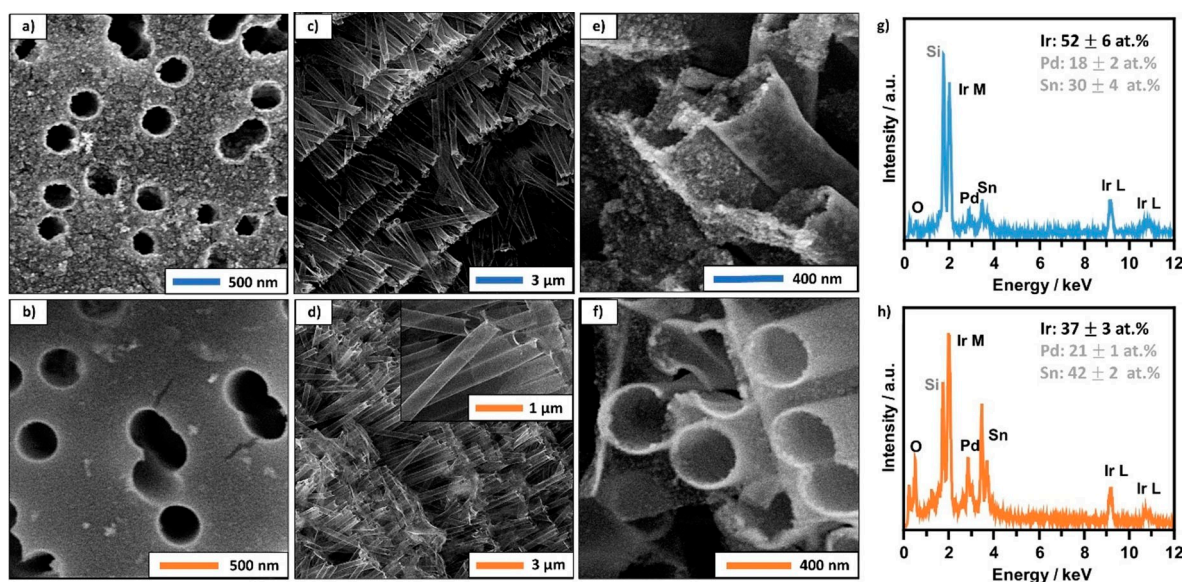


**Figure 3.** SEM images of the obtained Ir-deposits before (a, b) and after (c–f) removal of the PC membrane. The top and bottom row show the citrate- and EDA-deposits, respectively. The surface of the citrate-deposit (a) appears much rougher than its EDA-stabilized counterpart (b). After membrane removal, Ir-nanotubes are obtained (c–f). Those obtained from the EDA-solution exhibit a remarkably uniform wall-thickness (f). EDS-spectra recorded alongside SEM image acquisition (g, h) confirm the presence of Ir in both deposits.

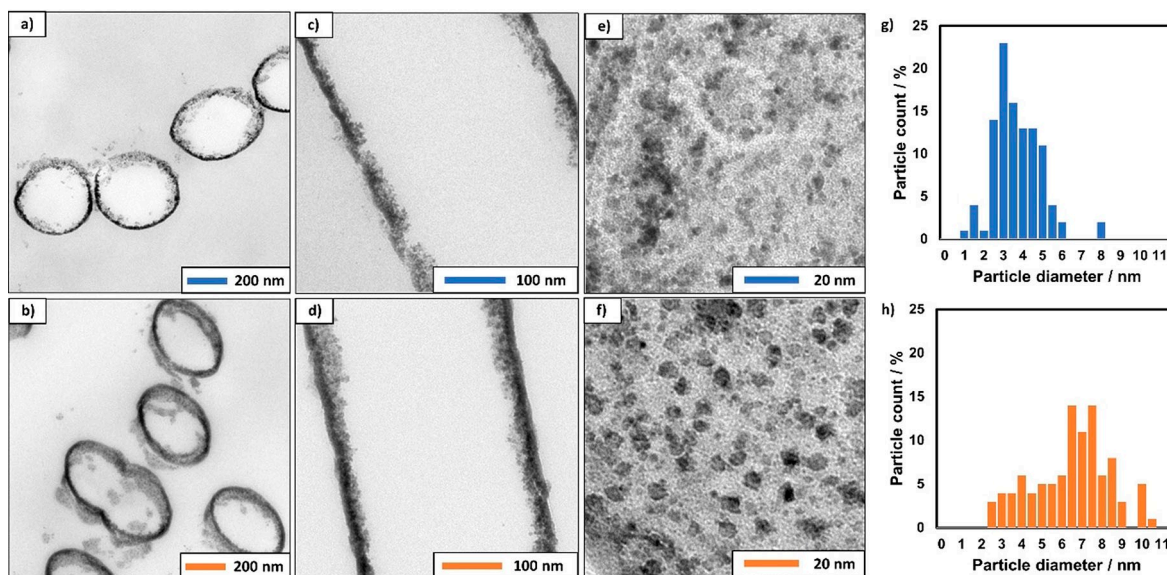


**Figure 4.** TEM-images of cross-sections perpendicular (a, b) and parallel (c, d) to the pore axis. Detail images (e, f) showing the granular character of the deposits. Subfigures (g, h) show the particle size distribution obtained from analyzing 100 particles from each sample.

overall smoother appearance of the deposit suggest that film growth is not primarily driven by the formation of new particles, but rather the deposition of Ir on the Pd-seeds and existing Ir-surfaces. This is likely caused by the more stable en-complex suppressing the assembly of Ir clusters and subsequent NP formation.

To clarify the valence state of the deposited material, XPS measurements were performed on as-prepared metallized PC membranes. Unfortunately, the EDA-deposit could not be measured properly, due to its lower film thickness and resulting low and inconsistent conductivity, causing considerable peak

broadening even under charge neutralization conditions. The XPS survey spectrum of the citrate deposit is displayed in Figure 5a. It is dominated by Ir and Sn, while less intense peaks of C, O, N and Pd can also be observed. A closer look on the Ir 4f region confirms the predominant deposition of metallic Ir (Figure 5b). The recorded peak maxima are situated at 63.8 eV and 60.8 eV for Ir 4f<sub>5/2</sub> and Ir 4f<sub>7/2</sub>, respectively. These values are in good accordance to the binding energies (BE) previously reported for metallic Ir.<sup>[82]</sup> Fitting of the Ir 4f region using parameters reported in the literature for pure Ir and IrO<sub>2</sub> surfaces<sup>[82]</sup> shows a strong metallic Ir signal (BE(Ir 4f<sub>5/2</sub>) = 63.9 eV;

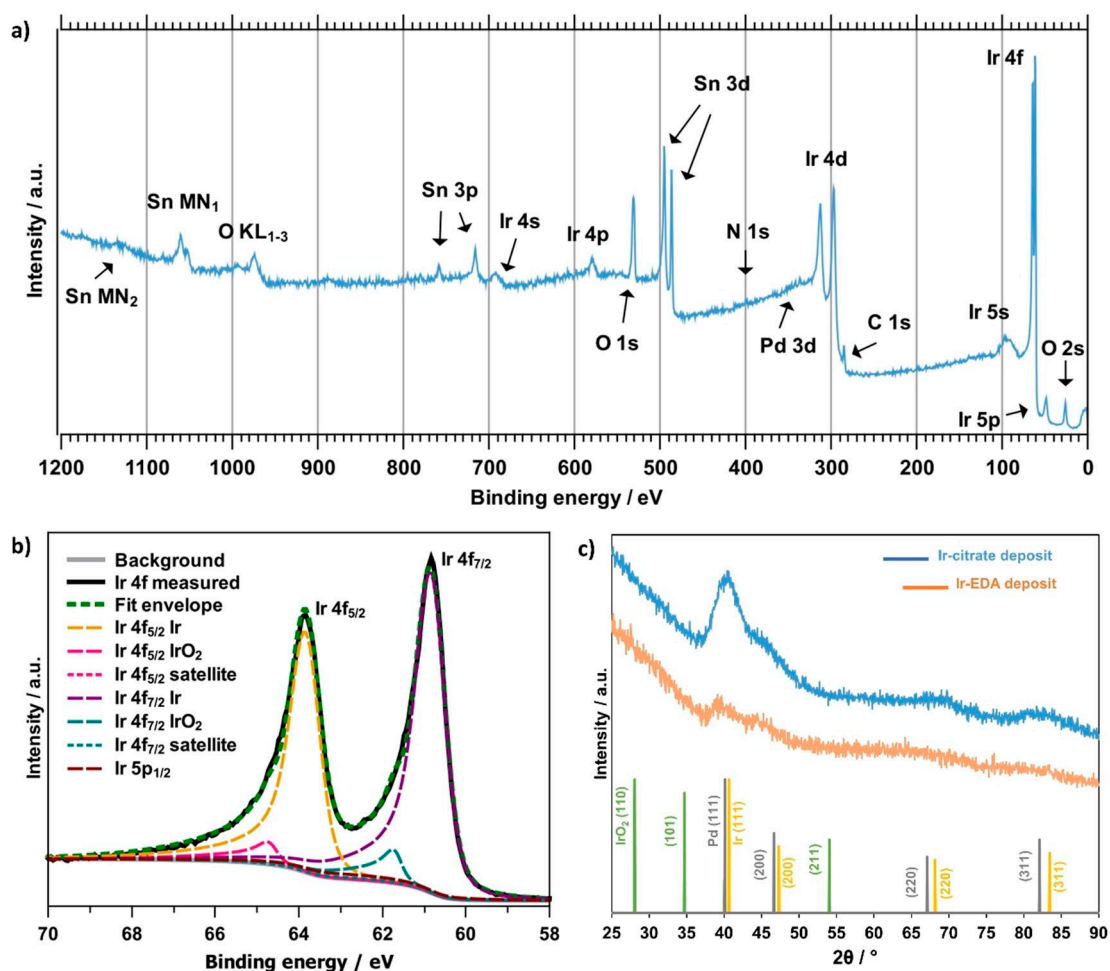


**Figure 5.** a) XPS survey spectrum of the Ir deposit plated using the citrate bath. b) Detailed spectrum of the Ir 4f peaks, confirming the predominant presence of metallic Ir. Peak fitting was performed using literature parameters.<sup>[82]</sup> c) XRD-patterns of Ir deposits from citrate and EDA-stabilized plating solutions. The absence of distinct IrO<sub>2</sub> reflexes further corroborates the deposition of metallic Ir. Reflex positions for IrO<sub>2</sub>, Ir and Pd according to PDF-2 cards 15–870, 6–598 and 46–1043, respectively.

BE(Ir 4f<sub>7/2</sub>) = 60.9 eV) with small contributions of IrO<sub>2</sub>, as indicated by smaller peaks shifted towards higher binding energies (BE(Ir 4f<sub>5/2</sub>) = 64.8 eV; BE(Ir 4f<sub>7/2</sub>) = 61.7 eV). A small amount of surface oxide species is to be expected, due to the high oxygen affinity of Ir and the storage and transport of the samples in air prior to the measurement.<sup>[83]</sup> The shape of the valence band region between 0 eV and 5 eV agrees well with a previous report on metallic Ir surfaces (see supporting information, Figure S2d).<sup>[84]</sup> In addition, the presence of states right until the Fermi level at 0 eV further corroborates the metallic character of the Ir deposit. Contributions from Pd in this range are unlikely, due to the overall low intensity of the Pd photoelectron signal (see supporting information, Figure S2a). This is particularly interesting, as the overall amount of Pd in the samples is in the range of 20 at.%, according to EDS analysis (Figure 3g, h). This discrepancy between surface selective and bulk measurements is in good agreement with the previously proposed growth mechanism (Figure 2) in which Ir deposition occurs autocatalytically on the Pd seeds, leading to their complete coverage by Ir. Considering the element-specific

inelastic mean free path of the photoelectrons,<sup>[85]</sup> complete attenuation of the Pd signal is expected at an Ir overcoating thickness of ~6 nm (see supporting information, section 2 for details). As such, the morphology of our deposit, which is characterized by Pd nanoparticles being either coated by Ir or covered by subsequently nucleating Ir NPs, supports the low XPS signal intensity of Pd. The relatively strong Sn peaks are shifted towards the higher binding energies present in SnO<sub>2</sub> (BE(Sn 3d<sub>3/2</sub>) = 494.7 eV; BE(Sn 3d<sub>5/2</sub>) = 486.3 eV; see supporting information, Figure S2b).<sup>[86]</sup> This is in line with the expected oxidation of Sn(II) to Sn(IV) resulting in Pd NP formation during the sensitization and activation procedure. As SnO<sub>2</sub>-containing areas without Pd seeds are not catalytically inducing Ir plating, a weaker attenuation of the Sn photoelectron signal is expected. A detailed scan of the O 1s region can be found in the supporting information (Figure S2c). Although it is difficult to interpret due to highly overlapping species, the peak position indicates the presence of metal oxides.

X-ray diffraction (XRD) patterns of both deposits are given in Figure 5c. Both samples show broad reflexes centered around



40°, 45°, 69° and 82°, which can be identified as the (111), (200), (220) and (311) reflexes of fcc-Ir, respectively. Due to the similar lattice parameters and large reflex width, they are likely superimposed with reflexes caused by the underlying Pd seeds. The reflex intensities are generally higher for the citrate deposit which is expected due to the larger film thickness. For both samples, the broad reflex width coincides with the nanoparticulate structure observed in TEM (Figure 4e, f). In all diffractograms no distinct reflexes of IrO<sub>2</sub> can be observed, which suggests that the Ir oxide found in the XPS spectra is likely too sparse and/or amorphous in nature to be detected.

In summary, our results strongly suggest that during electroless deposition, metallic Ir is deposited predominantly. Interestingly, a previous study investigating the interplay between Ir(III) and NaBH<sub>4</sub> reports that below a solution temperature of 40 °C no metallic Ir is formed, since the increase in pH caused by borohydride hydrolysis leads to the formation of IrO<sub>2</sub>, despite the reducing character of NaBH<sub>4</sub>.<sup>[13]</sup> This suggests, that in our case the stabilization of Ir(III) with citrate or EDA is able to sufficiently suppress oxide formation during plating, enabling the deposition of metallic Ir at room temperature.

### 2.3. Catalysis Experiments

The catalytic activity of the Ir-coated membranes is investigated using the reduction of 4-nitrophenol and MO as model reactions. Ion-track etched polymers coated with catalytically active metallic NPs have previously been investigated as potential catalysts in flow-reactors, showing very high 4-nitrophenol conversion rates.<sup>[28,32]</sup> Activity towards this reaction has been reported for many transition metals including Cu,<sup>[26]</sup> Au,<sup>[27,50,87]</sup> Ag,<sup>[32,88]</sup> Pd,<sup>[34,89]</sup> Pt<sup>[89,90]</sup> and Ru.<sup>[91]</sup> In the case of Ir, 4-nitrophenol reduction has been studied on dispersed NPs with mixed results regarding the activity.<sup>[64,90]</sup>

When transition-metal surfaces/NPs are used as catalyst, the reaction follows a Langmuir-Hinshelwood reaction mechanism.<sup>[61]</sup> (i) BH<sub>4</sub><sup>-</sup> reacts with the surface leading to the formation of surface hydrogen species which (ii) continue to react with adsorbed 4-nitrophenol to form 4-aminophenol. In the case of Ir-based catalysts where metallic Ir might be accompanied by small amounts of oxidized species, a previous study suggests that catalytic activity is enhanced by the formation of positively charged oxygen vacancies during the reaction between IrO<sub>x</sub> and NaBH<sub>4</sub>. These are assumed to be active sites for the adsorption of negatively charged 4-nitrophenolate ions, thus complementing the hydrogen adsorption on the metallic surfaces. Resultingly, IrO<sub>2</sub> alone did not show catalytic activity towards 4-nitrophenol reduction in the aforementioned study.<sup>[64]</sup> As NaBH<sub>4</sub> is usually provided in large excess, it is assumed that the reaction follows pseudo-first-order kinetics. The conversion of 4-nitrophenol can easily be monitored using UV-Vis spectroscopy since both the educt and product of the reaction show prominent, non-interfering absorption bands.

As shown in Figure 6a, the as-prepared 4-nitrophenol/NaBH<sub>4</sub>-solution shows prominent absorption around 400 nm

which can be attributed to the 4-nitrophenolate anion in alkaline solutions.<sup>[64]</sup>

For flow-catalysis, 5 ml of freshly prepared reaction solution were pumped through the Ir-coated membranes manually at a flow rate of 5 ml min<sup>-1</sup> using a syringe with an attached filter holder. UV-Vis spectra of the solutions after passing the membrane show a significant decrease in absorbance at 400 nm, while the absorption band at 300 nm indicates the formation of 4-aminophenol.<sup>[61]</sup> As the absorbance is proportional to the concentration (assuming Lambert-Beer's law), the fraction of converted educt can be determined by comparing the 400 nm absorbance before and after passing the membrane. This leads to 4-nitrophenol-conversions of 75 % and 80 % for the citrate- and EDA-deposits, respectively. It is worth pointing out that these high conversions are reached after a single pass, i.e. over a distance of only 25 μm. This indicates a remarkably high catalytic activity of the deposits, especially when the small overall volume of the catalyst membrane (~1.96 mm<sup>3</sup>) is considered. The samples also showed outstanding conversion in the degradation of MO by NaBH<sub>4</sub> (~93 % at 5 ml min<sup>-1</sup>, see supporting information, section 3).

Similar performances in flow catalysis have been reached using polymer membranes coated with Ag nanoplatelets. Here, near quantitative 4-nitrophenol conversions (98 %) are reached at a slightly lower flowrate of 4 ml min<sup>-1</sup>, albeit using a larger catalyst volume (12.6 mm<sup>3</sup>).<sup>[28]</sup>

Comparing these values with other reactor designs shows the remarkable performance of metal NP coated polymer membrane catalysts. As an example, hierarchical Au-sponges discussed in a previous report achieve merely 40 % conversion at 5 ml min<sup>-1</sup> utilizing a much larger catalyst volume of 1200 mm<sup>3</sup>.<sup>[50]</sup> In this case, large voids of several 100 μm diameter are present between the sponge struts, starkly contrasting the submicron channel architecture of our membrane, which allows for an immediate access of the wall surface by diffusion. Table 2 compares different metal NP based catalysts used in the flow catalysis of 4-nitrophenol reduction. However, it is worth mentioning that comparing catalytic activities in general is difficult, due to differences in reaction conditions like reactant concentrations and temperature.

To investigate the adhesion and catalytic stability of the obtained deposits, membranes of comparable size to those used in flow catalysis are submerged in 10 ml of reaction solution which is then vigorously agitated using a vortex mixer at 2400 rpm. This is to reproducibly expose the coated membranes to severe amounts of mechanical stress and promote continuous interaction between reactants and catalyst. After 5 min a UV-Vis spectrum is recorded to determine the 4-nitrophenol conversion. The cycle is then repeated with fresh reaction solution, 8 times in total. As shown in Figure 6b, no clear trend towards lower 4-nitrophenol conversion can be observed over 8 cycles, indicating that both catalysts can be reused multiple times without suffering from significant NP loss or poisoning, even under these harsh conditions. Again, both deposits show similar catalytic activities despite their obvious differences in morphology. It is worth pointing out that the overall performance of both samples is significantly lower than



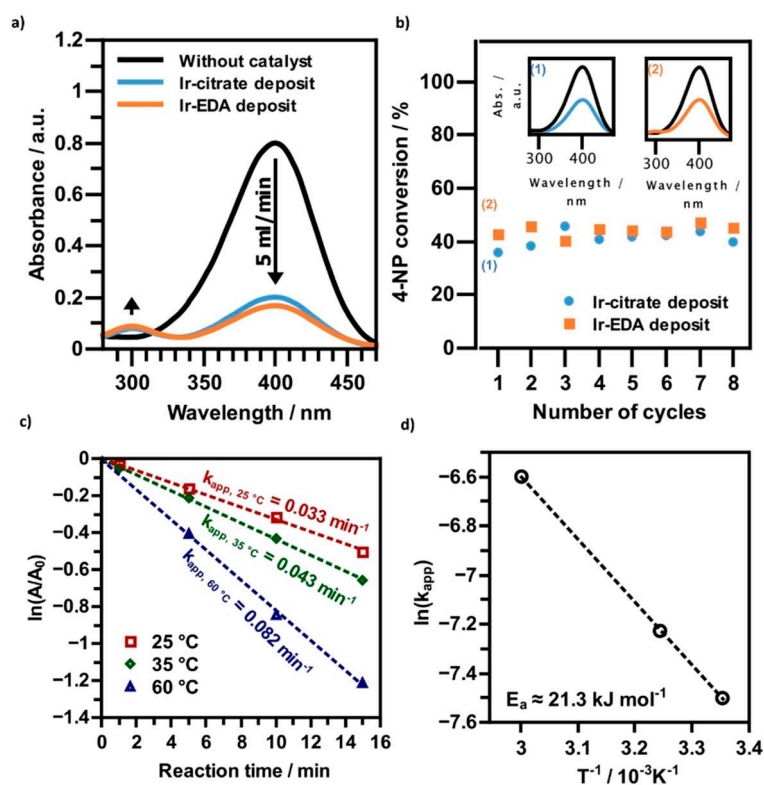


**Figure 6.** a) UV-Vis spectra of 4-nitrophenol/NaBH<sub>4</sub>-solutions before and after passing the Ir-coated membranes at a flow rate of roughly 5 ml min<sup>-1</sup>. A strong decrease in the 4-nitrophenol absorbance (400 nm) indicates a high catalytic activity of the deposits, while the appearing absorbance band at 300 nm suggests the formation of 4-aminophenol. b) 4-nitrophenol conversion over 8 cycles (5 min each, agitated at 2400 rpm) showing no clear trend of catalyst degradation. Insets 1 and 2 exemplarily show the UV-Vis spectra recorded before (black line) and after (orange/blue lines) the first cycles. c) Relative change of 4-nitrophenol absorbance during the catalyzed reaction, yielding the apparent rate constants ( $k_{app}$ ) at different temperatures. d) Arrhenius plot revealing the apparent activation energy  $E_a$  of the reaction.

**Table 2.** Comparison of different metal NP based catalysts used in 4-nitrophenol flow catalysis. The catalyst volume is the total volume of the carrier structure, without considering porosity. Differences in other reaction parameters like reactant concentrations and temperature are not considered here but might also influence the observed catalytic activity.

NP material	Carrier structure	Catalyst thickness and volume	4-nitrophenol conversion @ 5 ml min <sup>-1</sup> (or closest)	Ref.
Ir-NP film on Pd-seeds	lon-track etched PC	25 $\mu$ m ~1.96 mm <sup>3</sup>	75–80%	This work
Ag-nanoplatelets	lon-track etched PC	40 $\mu$ m 12.6 mm <sup>3</sup>	98% (4 ml/min)	[28]
Au-NPs on polymer-brushes	AAO	120 $\mu$ m 4.62 mm <sup>3</sup>	~95%	[27]
Ag-NPs	lon-track etched PC	30 $\mu$ m	67% (7 ml/min)	[32]
Hierarchical Au-sponge	Polymer foam	60 mm 1200 mm <sup>3</sup>	40%	[50]
Cu–Ag–Au <sub>2</sub> loaded protein fibrils	Nylon membrane	–	~40% (540 $\mu$ l/min)	[88]
Au-decorated polymeric monoliths	Fused silica capillary	45 mm 4.98 mm <sup>3</sup>	~60% (15 $\mu$ l/min)	[87]

when they are used in a flow-reactor setup. In static catalysis, after 5 min only ~40% of 4-nitrophenol is converted, while at least 75% conversion could be achieved in 2 min for the same volume using flow-catalysis. We ascribe this to the limited diffusion of reactants inside the pores. In addition, created products, in this case 4-aminophenol, could become enriched inside the pores and compete with incoming 4-nitrophenol. Both of these problems can be avoided by actively pushing the

solution through the membrane, making the whole surface available for reaction at all times. This shows that not only the composition and morphology of NP coatings is determining the catalytic activity, but also the applied mode of operation can significantly increase or decrease performance. In the case of our catalyst membrane, efficient access to its submicron pores is of paramount importance as they provide about 96% of the total catalyst surface (for details on the calculation see

supporting information, section 4). Due to the robustness of the deposit, sufficient reactant access can be conveniently achieved in a flow reactor, even at a comparatively high flow rate of 5 ml min<sup>-1</sup>.

To determine the apparent activation energy of the reaction, the relative absorbance change at 400 nm ( $A/A_0$ ) has been observed over time at different temperatures (Figure 6c), using the citrate-deposit as a catalyst. It appears that the reaction indeed follows the model for pseudo-first-order kinetics, showing a linear correlation between  $\ln(A/A_0)$  and the reaction time. The apparent rate constant  $k_{app}$  at 25 °C is 0.033 min<sup>-1</sup>, increasing to 0.043 min<sup>-1</sup> and 0.082 min<sup>-1</sup> at 35 °C and 60 °C, respectively. These values are in good accordance to a previous report on Ir NPs.<sup>[64]</sup> Using Arrhenius' equation, the change in apparent rate constant ( $k_{app}$ ) with temperature can be used to determine the apparent activation energy  $E_a$  of the catalyzed reaction, which amounts to roughly 21.3 kJ mol<sup>-1</sup> (Figure 6d). This value is located at the lower end of the wide range typically found for metal NPs (~10 to over 110 kJ mol<sup>-1</sup>),<sup>[61]</sup> corroborating the high activity of our deposits towards 4-nitrophenol reduction.

### 3. Conclusions

In this work we explored the possibilities of electroless Ir nanoplating by developing two plating baths suitable for the coating of complex 3D substrates. Our results show that by using suitable complexing agents, metastability of the solution can be maintained over the course of the plating reaction, enabling surface selective Ir NP film growth. The stability of the plating solutions is further corroborated by the absence of IrO<sub>2</sub> particle formation during both the thermally activated ligand exchange and plating in an alkaline environment. Conversely, due to the unusual complex inertness, large excess amounts of reducing agent still have to be employed to enable Ir reduction and reach acceptable reaction rates. Despite the need for optimization in terms of efficiency and plating speed, the presented plating protocols not only allow the dense NP-coating of membranes for flow-reactors, but also the template-based fabrication of filigree Ir nanotubes. This could provide ways for the optimization of existing Ir-based catalysts, by being able to densely coat more complex, high surface-area support structures or exploit the intrinsically high surface-to-volume ratio of metallic nanotubes. Finally, both deposits show remarkable activity towards the reduction of 4-nitrophenol, with the highest conversion rates being reached when the membranes are implemented in a flow-reactor setup.

### Experimental Section

Prior to use, all glassware was cleaned with boiling *aqua regia* and stored in an alkaline bath for at least two days. Aqueous solutions were freshly prepared using MilliQ-water (>18.2 MΩ cm). The following chemicals were used without further purification or modification: Iridium(III) chloride hydrate (*Alfa-Aesar*, 99.8%), sodium borohydrate (*Aldrich*, 99%), hydrochloric acid 37% (*PanReac*

*AppliChem*, for analysis), trisodium citrate dihydrate (*Alfa-Aesar*, 99%), ethylenediamine (*Fluka*, 99.5%), dichloromethane (*Roth*, ≥99.9%), tin(II) chloride dihydrate (*Sigma-Aldrich*, 98%), palladium(II) chloride (*Aldrich*, 99%), potassium chloride (*PanReac AppliChem*, USP, Ph.Eur.), methanol (*PanReac AppliChem*, pure), trifluoroacetic acid (*Sigma-Aldrich*, 99%), ethanol (*Labor-Service*, pure), 4-nitrophenol (*Fluka*, puriss. p.a.).

Commercially available hydrophilic ion-track etched polycarbonate membranes (*ipPore™*, *it4ip*, Louvain-la-Neuve, Belgium) with a nominal thickness of 25 μm, a pore diameter of 400 nm and pore density of 1.5 · 10<sup>8</sup> cm<sup>-2</sup> were used as substrates.

### Sensitization and Activation

Pd-seeds were deposited on the polycarbonate surface following a literature procedure.<sup>[34]</sup> In the present case, PC membranes were submerged in a Sn(II) containing sensitization solution (42 mM SnCl<sub>2</sub>, 71 mM trifluoroacetic acid) in methanol and water (1:1) for 45 min, after which they were washed with water and placed in an aqueous Pd(II) solution (11.3 mM PdCl<sub>2</sub>, 33.9 mM KCl). After 4 min, the membranes were again washed with water. Sensitization and activation were repeated two more times with the sensitization time shortened to 15 min. Afterwards, the membranes were washed again in water and ethanol and finally stored in water until the start of the deposition.

### Deposition of Ir NP Films

Ir NP films were deposited from two plating solutions featuring different stabilizers. Both solutions utilize hydrated IrCl<sub>3</sub> as metal source and NaBH<sub>4</sub> as reducing agent. The composition of both plating baths is given in Table 1. For the citrate-stabilized bath (solution 1), 10 mM IrCl<sub>3</sub> · H<sub>2</sub>O were dissolved in a solution of 40 mM trisodium citrate and 30 mM HCl. After a few minutes of ultrasonication the now clear greenish-yellow solution was heated to 80 °C in an oil bath. After 30 minutes the aged solution was placed in the fridge and allowed to cool down to about 7 °C. Immediately prior to the deposition the cooled down solution was mixed with an equal volume of freshly prepared 100 mM NaBH<sub>4</sub> solution. During the deposition, 50 mM NaBH<sub>4</sub> were added every 60 min. The EDA-stabilized plating solution (solution 2) was obtained by slowly adding cooled 6 mM IrCl<sub>3</sub> · H<sub>2</sub>O solution to an equal volume of cooled 36 mM EDA solution under constant stirring. The mixture was then heated to 70 °C and kept at that temperature for 60 min. After cooling down to room temperature, 60 mM NaBH<sub>4</sub> was added and replenished every 60 min during the plating reaction.

In both cases the Ir depositions were carried out at room temperature with the PC membranes fixed vertically in the solution. Solution 1 was replaced after 3 h and 6 h in order to prevent possible precipitates blocking the pores. Solution 2 did not show signs of homogeneous Ir NP nucleation even after 6 h, but was replaced after that time to avoid depletion due to the overall lower Ir-concentration.

### Catalysis Experiments

The reduction of 4-nitrophenol to 4-aminophenol in the presence of NaBH<sub>4</sub> has been chosen as a model reaction to investigate the catalytic activity of the synthesized Ir NP covered membranes. Experiments were conducted at room temperature both in a flow-reactor configuration, where the reaction solution is actively pushed through the membrane and in a conventional, stirred catalysis setup by submerging the membrane in the solution under constant agitation. In both cases the reaction solution was prepared

by adding 92.5  $\mu\text{l}$  of 5 mM 4-nitrophenol solution and 665  $\mu\text{l}$  of 500 mM  $\text{NaBH}_4$  solution to 10 ml of water. The final concentrations were 0.46 mM and 33.3 mM for 4-nitrophenol and  $\text{NaBH}_4$ , respectively. After thorough mixing the solution was either filled into a syringe for the flow-through reaction or in a test tube for the stability tests. In case of the flow-catalysis, the sample membrane was fixed inside a syringe filter holder (circular, inner diameter 10 mm) and the reaction solution was manually pushed through with a flowrate of approximately 5  $\text{ml min}^{-1}$ . UV-Vis spectra of the solution were recorded before and immediately after passing the membrane. The static mixing setup was used primarily to investigate adhesion stability and possible degradation of the catalyst. In that case, similarly sized, circular parts of the membrane (diameter 12 mm) were submerged in 10 ml of reaction solution in a 20 ml test tube which was then vigorously agitated using a vortex mixer at 2400 rpm. After 5 min of agitation, the UV-Vis spectrum of the solution was measured. For each sample, this procedure was repeated 8 times, using freshly prepared reaction solution for each cycle. For the activation energy investigations, 20 ml of freshly prepared reaction solution were filled in a beaker placed in an oil bath controlled by a thermostat. Reactions were performed using a  $\sim 1.5 \text{ cm}^2$  piece of catalyst membrane under constant stirring, while a small sample of the solution was temporarily removed in regular time intervals for recording UV-Vis spectra. Details on the MO degradation experiments can be found in the supporting information, chapter 3.

### Characterization

Scanning electron microscopy and EDS measurements were performed on a Philips XL30 FEG with an attached EDAX CDU LEAP EDS detector. Samples were investigated both before and after dissolution of the polycarbonate membrane. For the latter, samples were placed on conductive Si wafer pieces and fixed by applying a drop of dichloromethane (DCM). To completely remove the PC, the wafer pieces were then submerged in DCM for several hours.

For TEM measurements the coated membranes were embedded in *Araldite 502* resin (polymerization for 16 h at 60 °C) and subsequently cut into 70 nm slices using a Reichert Ultracut E ultramicrotome. The obtained samples were placed on a Cu grid and analyzed in a FEI CM20 TEM with an attached EDS detector (Oxford model 6767).

XRD patterns were recorded on as-prepared (membrane-embedded) samples in a Seifert XRD 3003 PTS diffractometer featuring a Cu anode (40 kV, 40 mA). The primary side contains a X-ray mirror while the beam is collimated on the secondary side using a long Soller slit. A graphite monochromator is used to separate the  $\text{CuK}\alpha$  line ( $\lambda \approx 1.542 \text{ \AA}$ ). Scans were performed in  $2\Theta/\Theta$ -geometry.

All XPS measurements were performed using a monochromatic X-ray source (Al  $\text{K}\alpha$ ) with an excitation energy of 1486.6 eV at a Thermo Fisher Escalab 250 spectrometer and a spot size of 650  $\mu\text{m}$ . Pass energies of 50 eV and 10 eV and step sizes of 0.1 eV and 0.05 eV with a dwell time of 50 ms per measurement point were used for the survey spectra and the detailed scans, respectively. The spectra were calibrated to the Fermi level of silver (0 eV), the binding energy of the Au  $4f_{7/2}$  emission line (84.0 eV), the Ag  $3d_{5/2}$  emission line (368.26 eV) and the Cu  $2p_{3/2}$  emission line (932.67 eV). Fitting was performed using CasaXPS with the fitting parameters adapted from Freakley *et al.*<sup>[82]</sup> The intensity ratio between the Ir  $4f_{7/2}$  and the Ir  $4f_{5/2}$  peak was confined to 4:3 and the ratio between the Ir  $4f_{7/2}$  and the Ir  $5p_{1/2}$  peak to 1:0.054, which is the ratio of the Scofield sensitivity factors of both emission lines.

UV-Vis measurements were conducted on a VWR UV-3100PC spectrophotometer. Quartz-cuvettes were used for analyzing the

plating solutions, while PE-cuvettes were used during the catalysis experiments and for analyzing the plating baths after  $\text{NaBH}_4$  addition.

### Acknowledgements

The authors thank the Structural Research Group at TU Darmstadt (FG Strukturforschung, Prof. W. Donner) for access to their XRD setup. M.C.S. acknowledges financial support through Deutsche Forschungsgemeinschaft (DFG) project number 406700532. Open access funding enabled and organized by Projekt DEAL.

### Conflict of Interest

The authors declare no conflict of interest.

**Keywords:** iridium · electroless plating · nanotubes · microreactors · 4-nitrophenol

- [1] W. M. Haynes, D. R. Lide, T. J. Bruno, *CRC Handbook of Chemistry and Physics, 95th Edition*, CRC Press, Boca Raton, 2014.
- [2] Y. Liu, B. Zhou, J. G. Zhu, *Sci. Rep.* **2019**, *9*, 1–7.
- [3] A. Etenko, T. McKechnie, A. Shchetkovskiy, A. Smirnov, *ECS Trans.* **2007**, *3*, 151–157.
- [4] M. S. Ureta-Zañartu, P. Bravo, J. H. Zagal, *J. Electroanal. Chem.* **1992**, *337*, 241–251.
- [5] S. Schlicht, S. Haschke, V. Mikhailovskii, A. Manshina, J. Bachmann, *ChemElectroChem* **2018**, *5*, 1259–1264.
- [6] M. H. Miles, E. A. Klaus, B. P. Gunn, J. R. Locker, W. E. Serafin, S. Srinivasan, *Electrochim. Acta* **1978**, *23*, 521–526.
- [7] J. Lim, S. Yang, C. Kim, C. W. Roh, Y. Kwon, Y. T. Kim, H. Lee, *Chem. Commun.* **2016**, *52*, 5641–5644.
- [8] M. S. Alia, B. Rasimick, C. Ngo, K. C. Neyerlin, S. S. Kocha, S. Pylypenko, H. Xu, B. S. Pivovar, *J. Electrochem. Soc.* **2016**, *163*, F3105–F3112.
- [9] M. S. Alia, S. Shulda, C. Ngo, S. Pylypenko, B. S. Pivovar, *ACS Catal.* **2018**, *8*, 2111–2120.
- [10] F. Bizzotto, J. Quinson, A. Zana, J. J. K. Kirkensgaard, A. Dworzak, M. Oezaslan, M. Arenz, *Catal. Sci. Technol.* **2019**, *9*, 6345–6356.
- [11] J. P. Contour, G. Pannetier, *J. Catal.* **1972**, *24*, 434–445.
- [12] S. E. Wood, J. T. Bryant, *Ind. Eng. Chem. Prod. Res. Dev.* **1973**, *12*, 117–122.
- [13] K. Chakrapani, S. Sampath, *Chem. Commun.* **2015**, *51*, 9690–9693.
- [14] H. Baida, P. Diao, *Rare Met.* **2012**, *31*, 523–530.
- [15] S. Kundu, H. Liang, *J. Colloid Interface Sci.* **2011**, *354*, 597–606.
- [16] M. Cui, Y. Zhao, C. Wang, Q. Song, *Microchim. Acta* **2016**, *183*, 2047–2053.
- [17] E. N. el Sawy, V. I. Birss, *J. Mater. Chem.* **2009**, *19*, 8244–8252.
- [18] J. Näther, F. Köster, R. Freudenberger, C. Schöberl, T. Lampke, *IOP Conf. Ser. Mater. Sci. Eng.* **2017**, *181*, 012041.
- [19] S. le Vot, L. Roué, D. Bélanger, *Electrochim. Acta* **2012**, *59*, 49–56.
- [20] M. A. el Khakani, B. le Drogoff, M. Chaker, *J. Mater. Res.* **1999**, *14*, 3241–3246.
- [21] Y. Gong, C. Wang, Q. Shen, L. Zhang, *Vacuum* **2008**, *82*, 594–598.
- [22] J. R. V. Garcia, T. Goto, *Mater. Trans.* **2003**, *44*, 1717–1728.
- [23] J. Hämäläinen, T. Hatanpää, E. Puukilainen, L. Costelle, T. Pilvi, M. Ritala, M. Leskelä, *J. Mater. Chem.* **2010**, *20*, 7669–7675.
- [24] J. Hämäläinen, T. Hatanpää, E. Puukilainen, T. Sajavaara, M. Ritala, M. Leskelä, *J. Mater. Chem.* **2011**, *21*, 16488–16493.
- [25] M. Ming, Y. Zhang, C. He, L. Zhao, S. Niu, G. Fan, J. S. Hu, *Small* **2019**, *15*, 1903057.
- [26] R. Bendi, T. Imae, *RSC Adv.* **2013**, *3*, 16279–16282.
- [27] J. Liu, S. Ma, Q. Wei, L. Jia, B. Yu, D. Wang, F. Zhou, *Nanoscale* **2013**, *5*, 11894–11901.
- [28] F. Muench, R. Popovitz-Biro, T. Bendikov, Y. Feldman, B. Hecker, M. Oezaslan, I. Rubinstein, A. Vaskevich, *Adv. Mater.* **2018**, *30*, 1805179.

- [29] P. Y. Apel, S. N. Dmitriev, *Adv. Nat. Sci. Nanosci. Nanotechnol.* **2011**, *2*, 013002.
- [30] Y. Yu, K. Kant, J. G. Shapter, J. Addai-Mensah, D. Losic, *Microporous Mesoporous Mater.* **2012**, *153*, 131–136.
- [31] A. B. Yeszhanov, A. A. Mashentseva, I. v. Korolkov, Y. G. Gorin, A. L. Kozlovskiy, M. v. Zdorovets, *Chem. Pap.* **2018**, *72*, 3189–3194.
- [32] F. Muench, M. Rauber, C. Stegmann, S. Lauterbach, U. Kunz, H. J. Kleebe, W. Ensinger, *Nanotechnology* **2011**, *22*, 415602.
- [33] S. R. Nicewarner-Peña, R. G. Freeman, B. D. Reiss, L. He, D. J. Peña, I. D. Walton, R. Cromer, C. D. Keating, M. J. Natan, *Science* **2001**, *294*, 137–141.
- [34] S. Schaefer, E. M. Felix, F. Muench, M. Antoni, C. Lohaus, J. Brötz, U. Kunz, I. Gärtner, W. Ensinger, *RSC Adv.* **2016**, *6*, 70033–70039.
- [35] T. Stohr, J. Brötz, M. Oezaslan, F. Muench, *Chem. Eur. J.* **2020**, *26*, 3030–3033.
- [36] H. Zhou, Z. Zhang, C. Jiang, G. Guan, K. Zhang, Q. Mei, R. Liu, S. Wang, *Anal. Chem.* **2011**, *83*, 6913–6917.
- [37] T. Walbert, M. Antoni, F. Muench, T. Späth, W. Ensinger, *ChemElectroChem* **2018**, *5*, 1087–1097.
- [38] F. Muench, E. M. Felix, M. Rauber, S. Schaefer, M. Antoni, U. Kunz, H. J. Kleebe, C. Trautmann, W. Ensinger, *Electrochim. Acta* **2016**, *202*, 47–54.
- [39] C. McKeown, F. M. F. Rhen, *J. Appl. Electrochem.* **2018**, *48*, 165–173.
- [40] L. Sun, D. Zhang, Y. Sun, S. Wang, J. Cai, *Adv. Funct. Mater.* **2018**, *28*, 1707231.
- [41] D. Sun, H. Zhang, X. Zhang, J. Yang, *ACS Appl. Mater. Interfaces* **2019**, *11*, 9621–9628.
- [42] J. Xu, X. Li, Y. Zhong, J. Qi, Z. Wang, Z. Chai, W. Li, C. Jing, Y. Cheng, *Adv. Mater. Technol.* **2018**, *3*, 1800372.
- [43] C. R. K. Rao, D. C. Trivedi, *Coord. Chem. Rev.* **2005**, *249*, 613–631.
- [44] J. Sudagar, J. Lian, W. Sha, *J. Alloys Compd.* **2013**, *571*, 183–204.
- [45] R. Weil, K. Parker, in *Electroless Plating: Fundamentals and Applications*, Reprint Edition (Eds.: G. O. Mallory, J. B. Hajdu), Noyes Publications/William Andrew Publishing LLC, **2009**, pp. 111–139.
- [46] F. Muench, B. Juretzka, S. Narayan, A. Radetinac, S. Flege, S. Schaefer, R. W. Stark, W. Ensinger, *New J. Chem.* **2015**, *39*, 6803–6812.
- [47] C. N. Grabill, D. Freppon, M. Hettinger, S. M. Kuebler, *Appl. Surf. Sci.* **2019**, *466*, 230–243.
- [48] Y. J. Song, J. R. Monnier, P. T. Fanson, C. T. Williams, *J. Catal.* **2014**, *315*, 59–66.
- [49] F. Muench, S. Schaefer, L. Hagelüken, L. Molina-Luna, M. Duerrschabel, H. J. Kleebe, J. Brötz, A. Vaskevich, I. Rubinstein, W. Ensinger, *ACS Appl. Mater. Interfaces* **2017**, *9*, 31142–31152.
- [50] Y. Yu, W. Xiao, T. Zhou, P. Zhang, C. Yan, Z. Zheng, *Mater. Chem. Front.* **2017**, *1*, 482–486.
- [51] R. N. Rhoda, *Trans. IMF* **1959**, *36*, 82–85.
- [52] Y. S. Cheng, K. L. Yeung, *J. Membr. Sci.* **2001**, *182*, 195–203.
- [53] P. Steinmetz, S. Alperine, A. Friant-Costantini, P. Josso, *Surf. Coat. Technol.* **1990**, *43–44*, 500–510.
- [54] T. Stohr, A. Fischer, F. Muench, M. Antoni, S. Wollstadt, C. Lohaus, U. Kunz, O. Clemens, A. Klein, W. Ensinger, *ChemElectroChem* **2020**, *7*, 855–864.
- [55] F. Muench, S. Kaserer, U. Kunz, I. Svoboda, J. Brötz, S. Lauterbach, H. J. Kleebe, C. Roth, W. Ensinger, *J. Mater. Chem.* **2011**, *21*, 6286–6291.
- [56] W. Diao, J. M. M. Tengco, A. M. Gaffney, J. R. Regalbuto, J. R. Monnier, in *Catalysis: Volume 32* (Eds.: J. Spivey, Y. Han, D. Shekhawat), Royal Society of Chemistry, **2020**, pp. 116–150.
- [57] H. Mori, S. Maezawa, K. Oguro, E. Torikai, U. S. patent 5865881, **1997**.
- [58] J. E. A. M. van den Meerakker, *J. Appl. Electrochem.* **1981**, *11*, 395–400.
- [59] X. Xia, L. Figueroa-Cosme, J. Tao, H. C. Peng, G. Niu, Y. Zhu, Y. Xia, *J. Am. Chem. Soc.* **2014**, *136*, 10878–10881.
- [60] L. Q. Zheng, X. D. Yu, J. J. Xu, H. Y. Chen, *Chem. Commun.* **2015**, *51*, 1050–1053.
- [61] P. Hervés, M. Pérez-Lorenzo, L. M. Liz-Marzán, J. Dzubiella, Y. Lu, M. Ballauff, *Chem. Soc. Rev.* **2012**, *41*, 5577–5587.
- [62] H. Gamsjäger, P. Beutler, *J. Chem. Soc. Dalton Trans.* **1979**, 1415–1418.
- [63] I. A. Poulsen, C. S. Garner, *J. Am. Chem. Soc.* **1962**, *84*, 2032–2037.
- [64] D. Xu, P. Diao, T. Jin, Q. Wu, X. Liu, X. Guo, H. Gong, F. Li, M. Xiang, Y. Ronghai, *ACS Appl. Mater. Interfaces* **2015**, *7*, 16738–16749.
- [65] Y. Zhao, E. A. Hernandez-Pagan, N. M. Vargas-Barbosa, J. L. Dysart, T. E. Mallouk, *J. Phys. Chem. Lett.* **2011**, *2*, 402–406.
- [66] I. Ohno, *J. Electrochem. Soc.* **1985**, *132*, 2323.
- [67] E. Keçeli, S. Özkaz, *J. Mol. Catal. A* **2008**, *286*, 87–91.
- [68] K. S. Krishna, C. S. S. Sandeep, R. Philip, M. Eswaramoorthy, *ACS Nano* **2010**, *4*, 2681–2688.
- [69] H. I. Schlesinger, H. C. Brown, H. R. Hoekstra, L. R. Rapp, *J. Am. Chem. Soc.* **1953**, *75*, 199–204.
- [70] D. M. F. Santos, C. A. C. Sequeira, *Renewable Sustainable Energy Rev.* **2011**, *15*, 3980–4001.
- [71] T. B. Field, J. L. McCourt, W. A. E. McBryde, *Can. J. Chem.* **1974**, *52*, 3119–3124.
- [72] E. N. Baker, H. M. Baker, B. F. Anderson, R. D. Reeves, *Inorg. Chim. Acta* **1983**, *78*, 281–285.
- [73] J. Reedijk, *Platinum Met. Rev.* **2008**, *52*, 2–11.
- [74] J. G. H. du Preez, C. Viviers, T. Louw, E. Hosten, H. Jonck, *Solvent Extr. Ion Exch.* **2004**, *22*, 175–188.
- [75] Y. M. L. de Jesús, A. Vicente, G. Lafaye, P. Marécot, C. T. Williams, *J. Phys. Chem. C* **2008**, *112*, 13837–13845.
- [76] H. Nawafune, S. Mizumoto, M. Haga, E. Uchida, *Trans. Inst. Met. Finish.* **1996**, *74*, 21–24.
- [77] S. Kida, *Bull. Chem. Soc. Jpn.* **1966**, *39*, 2415–2417.
- [78] R. A. Bauer, F. Basolo, *Inorg. Chem.* **1969**, *8*, 2237–2242.
- [79] R. A. Bauer, F. Basolo, *Inorg. Chem.* **1969**, *8*, 2231–2236.
- [80] G. W. Watt, L. E. Sharif, E. P. Helvenston, *Inorg. Chem.* **1962**, *1*, 6–9.
- [81] G. K. Schweitzer, L. L. Pesterfield, *The Aqueous Chemistry of the Elements*, Oxford University Press, Inc., New York, **2010**.
- [82] S. J. Freakley, J. Ruiz-Esquius, D. J. Morgan, *Surf. Interface Anal.* **2017**, *49*, 794–799.
- [83] D. Bhalothia, D. L. Tsai, S. P. Wang, C. Yan, T. S. Chan, K. W. Wang, T. Y. Chen, P. C. Chen, *J. Alloys Compd.* **2020**, *844*, 156160.
- [84] R. Koetz, H. Neff, S. Stucki, *J. Electrochem. Soc.* **1984**, *131*, 72–77.
- [85] M. P. Seah, W. A. Dench, *Surf. Interface Anal.* **1979**, *1*, 2–11.
- [86] M. A. Stranick, A. Moskwa, *Surf. Sci. Spectra* **1993**, *2*, 50–54.
- [87] A. M. Khalil, V. Georgiadou, M. Guerrouache, S. Mahouche-Chergui, C. Dendrinou-Samara, M. M. Chehimi, B. Carbonnier, *Polymer* **2015**, *77*, 218–226.
- [88] R. Huang, H. Zhu, R. Su, W. Qi, Z. He, *Environ. Sci. Technol.* **2016**, *50*, 11263–11273.
- [89] M. T. Islam, R. Saenz-Arana, H. Wang, R. Bernal, J. C. Noveron, *New J. Chem.* **2018**, *42*, 6472–6478.
- [90] F. Ramírez-Crescencio, R. Redón, A. Herrera-Gomez, G. Gomez-Sosa, M. Bravo-Sanchez, A. L. Fernandez-Osorio, *Mater. Chem. Phys.* **2017**, *201*, 289–296.
- [91] R. Ding, Q. Chen, Q. Luo, L. Zhou, Y. Wang, Y. Zhang, G. Fan, *Green Chem.* **2020**, *22*, 835–842.

Manuscript received: June 17, 2020  
Revised manuscript received: August 3, 2020